A Combined Approach for Monitoring Monthly Surface Water/Ice Dynamics of Lesser Slave Lake Via Earth Observation Data

Hatef Dastour 🄳, Ebrahim Ghaderpour 🄳, and Quazi K. Hassan 🄳

Abstract—Surface water/ice dynamic monitoring is crucial for many purposes, such as water resource management, agriculture, climate change, drought, and flood forecasting. New advances in remote sensing satellite data have made it possible to monitor the surface water/ice dynamics both spatially and temporally. However, there are many challenges when using these data, such as the availability of valid imagery, cloud contamination issues for Landsat-8, and sensitivity of Sentinel-1 C-band to wind speed, topography, and others. A combined methodology using Landsat-8 and Sentinel-1 synthetic aperture radar (SAR) data was proposed to create monthly change maps at 30-m spatial resolution for the Lesser Slave Lake in Alberta, Canada, for the period 2017–2020. The potentials of multispectral indices for Landsat-8, such as the normalized difference vegetation index (NDVI), normalized difference water index (NDWI), and modified NDWI (MNDWI) as well as the Sentinel-1 SAR backscattering coefficients (VV-VH) and normalized difference polarized index (NDPI) for separating water/ice from the land were investigated. The results obtained from satellite data with historical discharge and water level measurements for the lake were compared. Furthermore, the results show that the MNDWI and VH are the most effective indices for creating the change maps. The overall accuracies achieved for MNDWI and VH are 92.10% and 68.86% for cold months and 99.88% and 98.49% for warm months, respectively.

Index Terms—Landsat-8, lesser slave lake, monthly dynamic changes, sentinel-1, surface water areas, threshold-based classification.

I. INTRODUCTION

MONITORING surface lake dynamics is pivotal for lake resource management, drought, flood forecasting, and environmental construction [1]–[3]. Climate change and human

Hatef Dastour is with the Department of Geomatics Engineering, University of Calgary, 2500 University Drive, Calgary, AB T2N 1N4, Canada, and also with the Earth and Space Inc., Calgary, AB T2N 1N4, Canada (e-mail: hatef.dastour@ucalgary.ca).

Ebrahim Ghaderpour is with the Department of Geomatics Engineering, University of Calgary, 2500 University Drive, Calgary, AB T2N 1N4, Canada, also with the Department of Earth Sciences, Sapienza University of Rome, Piazzale Aldo Moro, 5, 00185 Rome, Italy, and also with the Earth and Space Inc., Calgary, AB T2N 1N4, Canada (e-mail: ebrahim.ghaderpour@ucalgary.ca).

Quazi K. Hassan is with the Department of Geomatics Engineering, University of Calgary, 2500 University Drive, Calgary, AB T2N 1N4, Canada (e-mail: qhassan@ucalgary.ca).

activities are two primary factors that may significantly impact lake acreage and cause inter and intraannual surface water distribution variation, influencing climate, agriculture, and human well-being [4]. Recently, remote sensing satellite data have made it possible to monitor the surface water at regional to global scales. However, it is still challenging to provide products with desired temporal and spatial accuracy for many applications, such as hydrology and agriculture [5].

Various types of imagery obtained by satellites with optical sensors have been used to monitor the surface lake including moderate resolution imaging spectroradiometer (MODIS) (250 and 500-m resolution), Landsat (30-m resolution), and Sentinel-2 (10-m resolution) imagery [6]–[9]. Two of the most common multispectral indices used for monitoring the surface lake dynamics are the normalized difference water index (NDWI) [10] and modification of normalized difference water index (MNDWI) [11]. The positive values of NDWI and MNDWI are typically used to classify water bodies [12]. The normalized difference vegetation index (NDVI) is another spectral index widely used for land cover and water surface monitoring [13], [14]. However, the main limitation of these indices is their sensitivity to cloud contamination. This limits the reliable use of data to only cloud-free conditions, heavily restricted in certain regions, e.g., in the tropics and high-latitude regions [15].

Synthetic aperture radar (SAR) has been widely used for monitoring surface water due to its insensitivity to sunlight and clouds. Radar sensors use longer wavelengths at the centimeter to meter scale, which gives the ability to see through clouds. SAR observations acquired from several sensors, such as RADARSAT [16] and Envisat ASAR [17] have been utilized for detecting floods and water surface monitoring. The C-band SAR data has also been utilized for operational wetland monitoring at high latitudes [18]. Creating a change map via these data was, however, limited due to a lack of observations and difficulty to access the data freely [12].

Upon the successful launch of Sentinel-1 satellites, the SAR observations have become freely available for educational and research purposes over large parts of the globe. The Sentinel-1 data has already shown a vigorous potential for detecting and monitoring open water bodies at high spatial and temporal resolutions (e.g., 10 m and 6-day over the boreal region) [12], [19]. The SAR backscattering coefficients used for water surface monitoring may have been altered due to the effect of

Fig. 1. Lesser Slave Lake in Alberta, Canada. The top panel is generated from https://www.simplemappr.net/. The elevation data (30 m) is provided by the U.S. Geological Survey. The basin boundaries and river shapefiles are provided by the Government of Canada at https://open.Canada.ca/data.
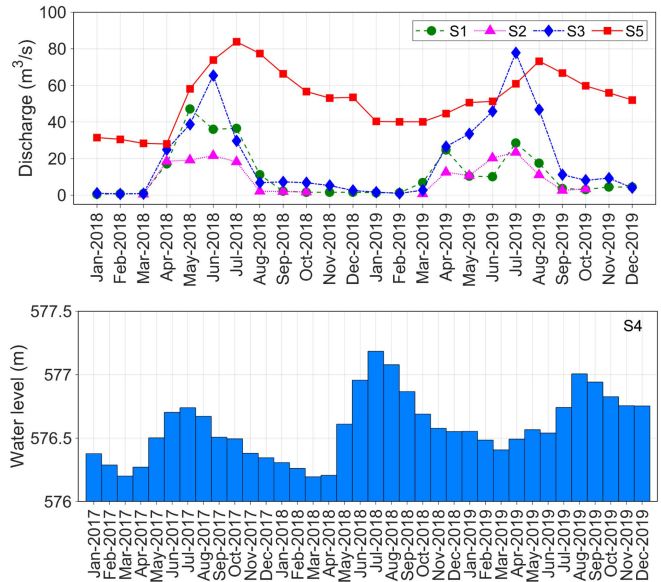

Fig. 2. Historical hydrological measurements. The top panel shows the discharge values measured at the hydrometric stations S1, S2, S3, and S5 displayed by red stars in Fig. 1. The bottom panel shows the water level in meters above the sea level for the Lesser Slave Lake measured at S4 displayed by the red star in Fig. 1.

the wind causing roughness on the surface of the water, making it very challenging for separating water from nonwater features reliably [19].

In this contribution, a combined threshold-based method is proposed to generate monthly change maps for water surface extend via satellite data. The Sentinel-1 SAR imagery is used for monitoring the water surface extent of the Lesser Slave Lake in Alberta, Canada [20]. The lake is located at a high latitude (about $55°$), where usable optical satellite imagery, such as Landsat-8 is very limited due to atmospheric conditions. The lake is in the central part of the Athabasca River Basin (ARB). The impact of climate change on streamflow in ARB is extensively studied via robust wavelet techniques by Ghaderpour et al. [21]. Herein, monthly images within the 2017–2020 period, separating water from nonwater pixels at 30-m resolution, are produced to visualize the dynamics of the water surface extend. The results are further assessed via ground-based measurements, including the discharge and water level. Since the Sentinel-1 SAR data became available just recently and the main focus here is employing the use of such data, this research was limited to the period of 2017–2020.

The rest of this article is organized as follows. The study region and datasets are described in Section II. The proposed methods including the statistical methods for model validation are presented in Section III. Section IV demonstrates the results and validation as well as challenges and comparisons with other techniques, and Section V concludes this article.

II. MATERIALS

A. Study Region

The Lesser Slave Lake is part of ARB, the second largest lake entirely within Alberta boundaries and located in central Alberta (Fig. 1). The lake is about 100-km long and 15 km at its widest point covering approximately 1160 km^2. The lake averages about 11 m in-depth and are 21 m at its deepest. The tributaries of the Lesser Slave Lake include the Assineau River, Driftpile River, Swan River, and South Heart River, the largest river flowing into the lake. The Lesser Slave Lake drains into the Athabasca River in an easterly direction for 72 km by way of the Lesser Slave River.

The Lesser Slave Lake is a popular place for birdwatching or birding. The Lesser Slave Basins provide a water supply for industrial, municipal, domestic, and agricultural users, and have provincially significant fishery and ecological values, particularly for the aboriginal peoples [20]. The large catchment area of the lake can cause significant fluctuations in water levels due to extreme runoff events.

B. Datasets and Preprocessing

The datasets analyzed herein include ground-based data, such as water flow, water level, and climate as well as remote sensing satellite data, such as Landsat-8 and Sentinel-1.

1) Water Flow and Water Level Data: The monthly water flow (discharge) and water level time series are provided freely by the Water Survey of Canada at https://wateroffice.ec.gc.ca. The time series were acquired from the hydrometric stations shown by red stars in Fig. 1 with their names mentioned in Table I along with their coordinates and drainage areas. This dataset was used for the assessment of the monitoring results. Fig. 2 exhibits the available monthly time series within the 2017–2020 period. Note that no water flow data were available for the years 2017 and 2020. At the time of conducting this research, the water level data for the lake was not available for 2020.

2) Climate Data: The temperature and precipitation time series are freely provided by the Alberta Agriculture and Forestry

TABLE I
HYDROMETRIC STATIONS SHOWN BY RED STARS IN FIG. 1 ALONG WITH THEIR GEOGRAPHIC COORDINATES AND DRAINAGE AREAS

Label	Station ID	Station Name	Latitude	Longitude	Drainage (km^2)
S1	07BF905	South Heart River Near Big Prairie Settlement	55°34′47″	−116°17′44″	6000
S2	07BH003	Driftpile River Near Driftpile	55°20′47″	−115°47′47″	835
S3	07BJ001	Swan River Near Kinuso	55°18′56″	−115°25′01″	1900
S4	07BJ006	Lesser Slave Lake at Slave Lake	55°18′20″	−114°46′17″	13600
S5	07BK001	Lesser Slave River at Slave Lake	55°18′17″	−114°45′22″	13600

at https://agriculture.alberta.ca/acis/. The time series is obtained at the township level (about 10-km resolution) and computed by a mathematical data interpolation procedure that weights up to the eight nearest station observations. The wind speed is also provided free of cost by the Alberta Agriculture and Forestry at https://acis.alberta.ca/weather-data-viewer.jsp. The weather stations are displayed by red squares in Fig. 1. The derived product is not an official version of the materials reproduced, nor as having been made in affiliation with or with the endorsement of the Government of Alberta. The wind speed and temperature time series are used herein to assess the reliability of Sentinel-1 images.

3) Landsat-8 Data: Landsat-8 satellite, launched on an Atlas-V rocket from Vandenberg Air Force Base in California on February 11, 2013, is one of the most recently launched Landsat satellite which carries the operational land imager (OLI) and the thermal infrared sensor (TIRS) instruments. Landsat-8 orbits the Earth in a sun-synchronous, near-polar orbit, at an altitude of 705 km with a 16-day repeat cycle [22]. Landsat 8 L1TP (Precision Terrain) surface reflectance products at 30-m spatial resolution are freely available in the U.S. Geological Survey (USGS). The images are atmospherically corrected via auxiliary data regained from the moderate resolution imaging spectroradiometer (MODIS), such as water vapor, ozone, and aerosol optical thickness, as well as a digital elevation, derived model. Due to several factors, such as sensor health and the capability of data reception and acquisition, the amount of Landsat data are not constant temporally and spatially among Landsat sensors [22]. There were 64 Landsat-8 L1TP surface reflectance products (collection 1) available to download from USGS within the 2017–2020 period covering the study region. Only bands 3 (Green), 5 (NIR-Infrared), 6 (SWIR-1), and the Pixel Quality Assessment (PQA) for each Landsat image were used herein. According to the product guide for Landsat-8 [23], the PQA pixel values for clear scenes are 322, 386, 834, 898, 1346, while they are 324, 388, 836, 900, 1348 for water, and 336, 368, 400, 432, 848, 880, 912, 944, 1352 for snow/ice. Moreover, according to the product guide for Landsat-8, the PQA pixel values 368, 432, 880, and 944 are mutual between cloud and snow/ice. This means that we cannot differentiate cloud and snow/ice if those PQA pixel values are observed. For this reason mainly, when it comes to training data, we ignored pixels whose PQA pixel value is 368, 432, 880, and 944.

By applying various analyses on the Landsat-8 dataset and visually inspecting the images, almost no image was found whose PQA pixel values showed both clear and snow/ice. For this reason, the analyses were divided into two groups. Therefore, we identified that images from months November, December,

TABLE II
COLD MONTHS AND WARM MONTHS GROUPS

Group	Months
Cold Months	November, December, January, February, March, April
Warm Months	May, June, July, August, September, October

TABLE III
TRAINING LANDSAT-8 IMAGERY SELECTED FOR WARM MONTHS (A) AND COLD MONTHS (B)

(a) Cold months

#	Acquisition Date	Clear %	Water %	Snow/Ice %	Unusable %
1	6 February 17	7.62	0.16	74.10	18.12
2	9 February 18	0.17	0.05	85.14	14.64
3	13 March 18	1.49	0.00	73.08	25.43
4	29 March 18	0.04	0.00	97.62	2.34
5	14 April 18	2.19	0.12	89.80	7.89
6	30 April 18	57.73	0.32	36.33	5.62
7	12 February 19	0.06	0.02	74.94	24.98
8	28 February 19	5.72	0.05	94.17	0.06
9	16 March 19	4.70	0.01	90.79	4.50
10	18 March 20	0.99	0.00	94.05	4.96
11	3 April 20	0.04	0.01	94.67	5.28
12	17 February 21	3.47	0.06	82.05	14.42
13	21 March 21	7.44	0.01	88.46	4.09
14	6 April 21	11.27	0.03	49.41	39.29

(b) Warm months

#	Acquisition Date	Clear %	Water %	Snow/Ice %	Unusable %
1	29 May 17	61.36	38.64	0.00	0.00
2	30 June 17	37.27	26.00	0.00	36.73
3	17 June 18	43.18	29.93	0.00	26.89
4	19 July 18	47.62	38.59	0.00	13.79
5	19 May 19	61.26	38.74	0.00	0.00
6	22 July 19	61.13	38.57	0.00	0.30
7	24 September 19	39.11	35.70	0.00	25.19
8	10 October 19	57.28	37.79	0.00	4.93
9	24 July 20	35.42	31.20	0.00	33.38
10	9 August 20	59.71	38.58	0.00	1.71
11	25 August 20	35.57	29.71	0.00	34.72
12	10 September 20	60.97	39.03	0.00	0.00

January, February, March, and April mainly contained pixels whose PQA values showed clear and snow/ice. This group was labeled as Cold Months. Moreover, we also uncovered that images from months May, June, July, August, September, and October only contained pixels whose PQA values showed clear and water. This group was labeled as (open) Warm Months. Table II highlights the months considered for each of these two groups.

For each of the groups above, the cold months and the (open) warm months, a set of Landsat-8 images was selected
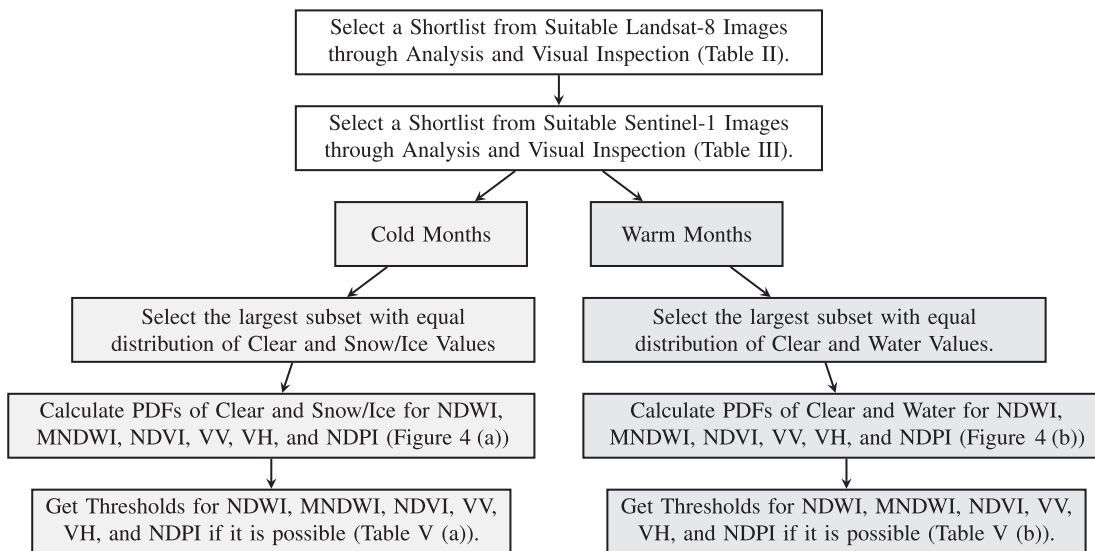
Fig. 3. Workflow of threshold selection.

TABLE IV
TRAINING SENTINEL-1 IMAGERY WHOSE ACQUISITION DATES ARE THE
CLOSET TO THE ACQUISITION DATES OF THE SELECTED LANDSAT-8 IMAGERY
ALONG WITH THE CLIMATE INFORMATION FOR THE COLD MONTHS (A) AND
THE WARM MONTHS (B)

(a) Cold months

#	Acquisition Date	Air Temp. Min. (°C)	Air Temp. Max. (°C)	Wind Speed Avg. (km/h)
1	1 March 17	-22.58	-12.12	9.55
2	7 February 18	-25.07	-14.69	3.95
3	15 March 18	-7.53	4.13	5.45
4	27 March 18	-11.67	-6.28	9.65
5	15 April 18	-3.77	8.15	5.25
6	2 May 18	3.20	16.11	11.25
7	14 February 19	-28.15	-14.26	4.40
8	26 February 19	-23.04	-7.00	10.40
9	17 March 19	-1.59	8.50	10.85
10	16 March 20	-16.15	0.74	5.90
11	4 April 20	-19.36	-2.02	7.65
12	15 February 21	-25.32	-15.44	11.55
13	23 March 21	-14.27	0.81	6.70
14	4 Apr 21	-1.17	6.69	11.70

(b) Warm months

#	Acquisition Date	Air Temp. Min. (°C)	Air Temp. Max. (°C)	Wind Speed Avg. (km/h)
1	31 May 17	10.85	23.84	9.70
2	24 June 17	7.93	21.19	7.90
3	19 June 18	13.04	29.36	5.85
4	20 July 18	10.49	20.49	8.65
5	21 May 19	3.38	20.54	9.10
6	20 July 19	10.88	22.19	6.75
7	25 September 19	6.04	10.72	10.80
8	12 October 19	-0.57	10.51	5.65
9	26 July 20	11.17	23.50	11.15
10	2 August 20	14.10	28.33	6.05
11	19 August 20	10.16	22.79	8.05
12	12 September 20	1.73	9.97	5.00

through various analyses using the PQA pixel values and visual inspections. Table III highlights the selected Landsat-8 images for the cold months and the warm months. In this table, Clear %, Water %, and Snow/Ice %, respectively, show the percentage of clear, water, and snow/ice pixels. Moreover, Unusable % shows, the percentage of pixels whose PQA values were not among clear, water, and snow/ice values. For the reasons mentioned above, we regarded pixels with the PQA pixel value of 368, 432, 880, and 944 also as unusable pixels. In addition, other images had very poor scene visibility and were almost fully contaminated, so those images were not considered herein.

4) Sentinel-1 Data: The Sentinel-1 constellation includes two radar satellites, namely, Sentinel-1A and B, launched by the European Space Agency (ESA) in April of 2014 and 2016, respectively. Sentinel-1 satellites are in near-polar, sun-synchronous orbits that provide continuous all-weather, day-and-night imagery at C-band (center frequency 5.405 GHz) in both singular and dual polarization. The repeat cycle of a single Sentinel-1 satellite is twelve days, while a six-day exact repeat cycle at the equator can also be achieved with the two satellites. The revisit rate is greater at higher latitudes due to the orbit track spacing variation with respect to latitude. The Sentinel-1 C-band synthetic aperture radar ground range detected (SAR-GRD) used herein was provided by the Copernicus coordinated and managed by the European Commission in partnership with the European Space Agency (ESA). Herein, the Level-1 GRD images at 10-m pixel spacing were used which belonged to the interferometric wide (IW) mode with single copolarization (VV: vertical transmit/vertical receive) and dual-band cross-polarization (VH: vertical transmit/horizontal receive). The images were processed using the Sentinel-1 Toolbox to generate a calibrated, ortho-corrected product. More precisely, each scene covering the study region was pre-processed by the Sentinel-1 Toolbox following three steps: 1) Thermal noise removal, (2) Radiometric calibration, and (3) Terrain correction using Shuttle Radar Topography Mission (SRTM) and then converted into decibels (dB) via the log scaling $10 \log 10(x)$.

In this study, 98 ascending and 217 descending SAR imagery within the 2017–2020 period were downloaded from the Google Earth Engine (GEE) with the implemented preprocessing steps mentioned above and at 30-m spatial resolution to match the resolution of Landsat-8 imagery, where each image
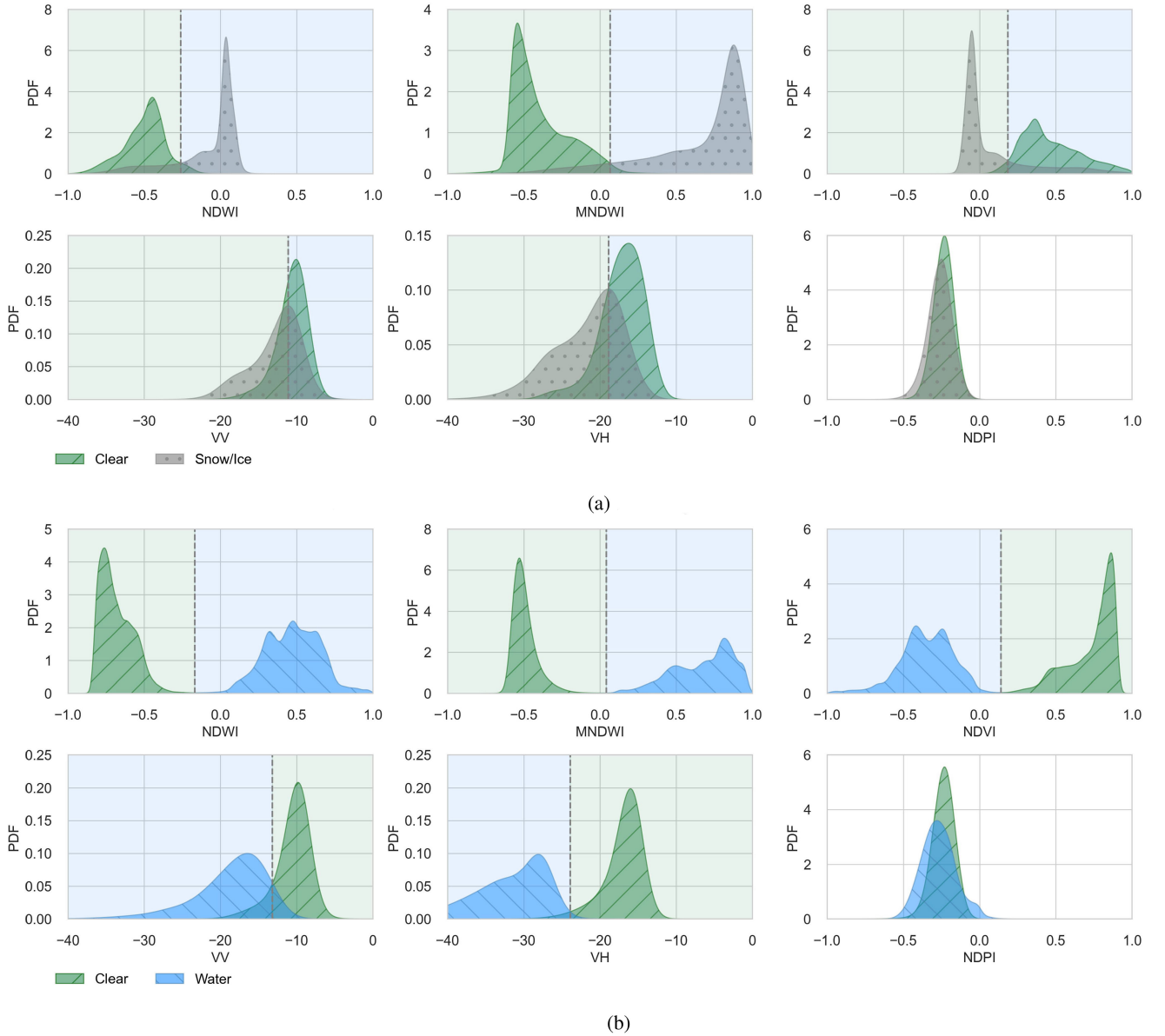
Fig. 4.   The normally distributed probability density curves of NDWI, MNDWI, NDVI, VV, VH, and NDPI. (a) For separating clear and Snow/Ice during the cold months. (b) For separating clear and water during the warm months.

had backscattering coefficient bands at VV and VH polarization. The Sentinel-1 images were then spatially aligned (pixelwise) with the Landsat-8 images via a median approach. Therefore, the shape of each Landsat-8 or Sentinel-1 image clipped to the study region was 1102×2997.

Table IV highlights the selected Sentinel-1 images for the cold months (a) and the warm months (b), respectively. These images were selected in a way that their acquisition dates were the closest to the corresponding Landsat-8 images. All images, except image #1 from Table III (a) were from descending satellite.

III. METHODOLOGY

In this section, the multispectral and SAR indices for Landsat-8 and Sentinel-1 SAR data are presented, respectively. Then,

a combined threshold-based methodology is described, and finally, some common statistical methods for validation are explained.

A. Multispectral Indices

The three multispectral indices NDWI, MNDWI, and NDVI are defined as

$$\text{NDWI} = \frac{\rho_{\text{Green}} - \rho_{\text{NIR}}}{\rho_{\text{Green}} + \rho_{\text{NIR}}} \tag{1}$$

$$\text{MNDWI} = \frac{\rho_{\text{Green}} - \rho_{\text{SWIR}}}{\rho_{\text{Green}} + \rho_{\text{SWIR}}} \tag{2}$$

$$\text{NDVI} = \frac{\rho_{\text{NIR}} - \rho_{\text{Red}}}{\rho_{\text{NIR}} + \rho_{\text{Red}}} \tag{3}$$

where ρ_{Green} (0.56 μm), ρ_{NIR} (0.86 μm), and ρ_{SWIR} (1.61 μm) are the reflections in the green, near-infrared, and short-wave infrared spectra, respectively [10], [11]. Some studies have shown that MNDWI can enhance the open water features better than the NDWI, i.e., it can more accurately discriminate water from nonwater features, especially for regions with many built-up land areas in the background [11].

B. SAR Indices

We used the VV and VH polarization in dB, and we investigated the potential of the normalized difference polarized index (NDPI) defined as [24], [25]

$$\mathrm{NDPI} = \frac{\mathrm{VV} - \mathrm{VH}}{\mathrm{VV} + \mathrm{VH}}. \tag{4}$$

C. Threshold-Based Classification

For an independent sample $\{x_1, x_2, \ldots, x_n\}$, the kernel density estimation can be defined as follows:

$$\widehat{f}_h(x) = \frac{1}{nh} \sum_{i=1}^{n} K\left(\frac{x - x_i}{h}\right) \tag{5}$$

where K is the kernel which is a nonnegative function, and h is a positive defines smoothness of the density plot (the bandwidth) [26], [27]. Here, kernel density estimation (KDE) with bandwidth $h = 0.1$ and the Gaussian kernel density [28] was employed to estimate the probability density function (PDF) for NDWI, MNDWI, NDVI, VV, VH, and NDPI.

These PDFs were used to define thresholds for separating clear and water pixels during the warm months, and snow/ice and clear during the cold months. For instance, for separating clear and water pixels during the warm months, first, a shortlist from suitable Landsat-8 images through analysis and visual inspection is selected (Table II), and then a shortlist from suitable sentinel-1 images through analysis and visual inspection (Table III) was chosen as well. Using these two sets, a dataset whose rows are from VV and VH polarizations (from sentinel-1 images) and corresponding PQA pixel value (from Landsat-8 images). Then, the largest subset with equal distribution of clear and water Values is selected. For calculation of the thresholds, let $\widehat{f}_h^c$ and $\widehat{f}_h^w$ represent kernel density estimations for rows the largest subset whose PQA value shows clear and water, respectively. Then, if possible, solving $\widehat{f}_h^c(x) = \widehat{f}_h^w(x)$ for x provides the thresholds for separating clear and water pixels during the warm months.

Fig. 3 summarizes the workflow of threshold selection. Moreover, Fig. 4 shows the normally distributed probability density curve of NDWI, MNDWI, NDVI, VV, VH, and NDPI for separating clear and snow/ice pixels during the cold months, and separating clear and water pixels during the warm months. In this figure, each dashed grey line represents the solution of the following equation:

$$\widehat{f}_h^c(x) = \widehat{f}_h^w(x) \quad (\text{or } \widehat{f}_h^c(x) = \widehat{f}_h^s(x)) \tag{6}$$

with $\widehat{f}_h^s$ representing the KDE for snow/ice values. Observe that, in the case of NDPI, there is too much overlap between

TABLE V
THRESHOLDS FOR VARIOUS MULTISPECTRAL INDICES (A) AND VV AND VH POLARIZATIONS (B)

(a) Thresholds for various multi-spectral indices

Group	Multispectral Index	Threshold
Cold Months	NDWI	-0.259
	MNDWI	0.065
	NDVI	0.185
Warm Months	NDWI	-0.169
	MNDWI	0.041
	NDVI	0.141

(b) Thresholds for VV and VH polarizations

Group	Backscattering Coefficients	Threshold
Cold Months	VV	-11.131
	VH	-18.894
Warm Months	VV	-13.168
	VH	-23.904

the PDF of water (or snow/ice) and clear. Thus, the threshold classification through NDPI was neglected.

In addition, Table V highlights thresholds for various multispectral indices and VV and VH polarizations for the cold and the warm months. Then, we used these thresholds for threshold-based classification methods to separate clear and snow/ice pixels during the cold months, and clear and water pixels during the warm months.

D. Accuracy Evaluation

To compare our threshold-based classification methods, a number of accuracy metrics were used including precision, recall, f1-score, and overall accuracy score [29], [30]. These metrics are defined as

$$\text{Precision} = \frac{TP}{TP + FP} \tag{7}$$

$$\text{Recall} = \frac{TP}{TP + FN} \tag{8}$$

$$\text{F1} = 2 \times \frac{\text{Precision} \times \text{Recall}}{\text{Precision} + \text{Recall}} \tag{9}$$

$$\text{Overall Accuracy} = \frac{TP + TN}{TP + FN + FP + TN} \tag{10}$$

where TP, FN, FP, and TN represent true positives, false negatives, false positives, and true negatives, respectively.

Table VI demonstrates the results of the metrics above for our threshold classification methods using NDWI, MNDWI, NDVI, VV, and VH for the cold months and warm months. In these tables, the weighted average for each metric was calculated through the number of instances of each class, and κ represents Cohen's Kappa. For binary classifications, the Cohen's Kappa formula is [29]

$$\kappa = \frac{2 \times (TP \times TN - FN \times FP)}{D} \tag{11}$$

TABLE VI
PRECISION, RECALL, F1-SCORE AND COHEN'S KAPPA SCORE (κ) FOR THRESHOLD-BASED CLASSIFICATIONS FOR THE COLD MONTHS (A) AND THE WARM MONTHS (B)

(a) Cold months

| | NDWI | | | | | MNDWI | | | | |
	Precision	Recall	F1-Score	κ	Accuracy	Precision	Recall	F1-Score	κ	Accuracy
Clear	0.262	0.993	0.415			0.502	0.975	0.663		
Snow/Ice	0.999	0.759	0.862			0.998	0.916	0.955		
Weighted Avg.	0.941	0.777	0.827			0.958	0.921	0.932		
Overall				0.331	0.777				0.623	0.921
	NDVI					VV				
	Precision	Recall	F1-Score	κ	Accuracy	Precision	Recall	F1-Score	κ	Accuracy
Clear	0.247	0.986	0.396			0.142	0.656	0.233		
Snow/Ice	0.998	0.741	0.851			0.953	0.637	0.764		
Weighted Avg.	0.939	0.760	0.814			0.885	0.639	0.719		
Overall				0.308	0.760				0.111	0.639
	VH									
	Precision	Recall	F1-Score	κ	Accuracy					
Clear	0.181	0.769	0.293							
Snow/Ice	0.970	0.681	0.800							
Weighted Avg.	0.904	0.689	0.758							
Overall				0.182	0.689					

(b) Warm months

| | NDWI | | | | | MNDWI | | | | |
	Precision	Recall	F1-Score	κ	Accuracy	Precision	Recall	F1-Score	κ	Accuracy
Clear	0.999	0.999	0.999			0.999	0.997	0.998		
Water	0.998	0.999	0.999			0.996	0.998	0.997		
Weighted Avg.	0.999	0.999	0.999			0.998	0.998	0.998		
Overall				0.998	0.999				0.995	0.998
	NDVI					VV				
	Precision	Recall	F1-Score	κ	Accuracy	Precision	Recall	F1-Score	κ	Accuracy
Clear	0.998	0.999	0.998			0.954	0.884	0.918		
Water	0.998	0.997	0.998			0.851	0.939	0.893		
Weighted Avg.	0.998	0.998	0.998			0.911	0.907	0.907		
Overall				0.996	0.998				0.811	0.907
	VH									
	Precision	Recall	F1-Score	κ	Accuracy					
Clear	0.997	0.977	0.987							
Water	0.968	0.996	0.982							
Weighted Avg.	0.985	0.985	0.985							
Overall				0.969	0.985					

Note that NDPI was excluded due to its poor performance in separating water or snow/ice from clear (See Fig. 4).

where $D = (TP + FP) \times (FP + TN) + (TP + FN) \times (FN + TN)$.

From Table VI (a), we observe that MNDWI and VH polarization, for threshold classification utilizing Landsat-8 and Sentinel-1 images, respectively, have the best-weighted average and overall accuracy scores among all. Similarly, from Table VI (b), it can be observed that NDWI and VH polarization have the best-weighted average and overall accuracy scores across all.

Moreover, as we demonstrated in Table VI, the accuracy of our classifications for separating water and clear pixels during the warm months utilizing the VH polarization was slightly higher than that of the VV polarization. Therefore, this confirmed that the VH polarization was more sensitive to the presence of surface water than the VV polarization. These results were consistent with the the conclusion found by Binh Pham-Duc et al. [12] and Liwei Xing et al. [19].

In addition, Table VII(a) shows confusion matrices from the threshold-based classification method for separating clear and snow/ice during the cold months. Likewise, Table VII(b) demonstrates confusion matrices from the threshold-based classification method for separating clear and water during the warm months.

E. Effect of Wind Speed on VV and VH Polarizations

Thresholds for VV and VH polarizations, obtained utilizing PDF and Sentinel-1 images, for the cold months and the warm months were provided in Table V. These thresholds were applied for threshold-based classification methods to separate clear and snow/ice pixels during the cold months, and clear and water pixels during the warm months.

For the study region, it was discovered that the wind speed was not a significant factor in identifying these thresholds although wind can cause roughness on the surface of the water [12], [19]. To see this, Sentinel-1 (Descending) images were separated by average wind speed within the study region. Then, thresholds for VV and VH polarizations for the cold and warm months were identified. These thresholds are available in Table VIII.

In Fig. 5, a linear relationship between average wind speed and threshold for VV/VH polarizations during the cold months [Fig. 5(a)] and the warm months [Fig. 5(b)] is demonstrated. Pearson correlation [31] between average wind speed and threshold for VV and VH polarizations is shown with r. As illustrated in the figure, all approximated slopes are small values and the Pearson correlation r between every two variables (wind speed

TABLE VII
CONFUSION MATRICES FOR NDWI, MNDWI, NDVI, VV, AND VH FOR THE COLD MONTHS (A), AND THE WARM MONTHS (B)

(a) Cold Months

NDWI

True Classes	Predicted Classes	
	Clear	Snow/Ice
Clear	3112915 / 0.994	20383 / 0.007
Snow/Ice	8753817 / 0.241	27508737 / 0.759

MNDWI

True Classes	Predicted Classes	
	Clear	Snow/Ice
Clear	3054629 / 0.975	78669 / 0.025
Snow/Ice	3029872 / 0.084	33232682 / 0.916

NDVI

True Classes	Predicted Classes	
	Clear	Snow/Ice
Clear	3089843 / 0.986	43455 / 0.014
Snow/Ice	9397559 / 0.259	26864995 / 0.741

VV

True Classes	Predicted Classes	
	Clear	Snow/Ice
Clear	2228535 / 0.656	1170876 / 0.344
Snow/Ice	13472885 / 0.363	23669450 / 0.637

VH

True Classes	Predicted Classes	
	Clear	Snow/Ice
Clear	2612954 / 0.769	786457 / 0.231
Snow/Ice	11835879 / 0.319	25306456 / 0.681

(b) Warm Months

NDWI

True Classes	Predicted Classes	
	Clear	Water
Clear	19788632 / 0.999	22163 / 0.001
Water	16887 / 0.001	13806532 / 0.999

MNDWI

True Classes	Predicted Classes	
	Clear	Water
Clear	19756910 / 0.997	53885 / 0.003
Water	21727 / 0.002	13801692 / 0.998

NDVI

True Classes	Predicted Classes	
	Clear	Water
Clear	19788827 / 0.999	21968 / 0.001
Water	37993 / 0.003	13785426 / 0.997

VV

True Classes	Predicted Classes	
	Clear	Water
Clear	17512916 / 0.884	2298863 / 0.116
Water	845217 / 0.061	13108094 / 0.939

VH

True Classes	Predicted Classes	
	Clear	Water
Clear	19352127 / 0.977	459652 / 0.023
Water	48881 / 0.004	13904430 / 0.997

Note That NDPI Was Excluded Due to Its Poor Performance in Separating Water or Snow/Ice From Clear (See Fig. 4).

average and thresholds for VV/VH polarization) were insignificant. As there was no notable linear relationship between wind speed average and thresholds for VV/VH polarizations (for our study region), we identified that wind speed was not a significant factor in our study.

F. Change Map Methodology

Threshold classification was utilized for generating spatiotemporal distribution maps of clear, water, and snow/ice for each month from 2017 to 2020. In doing so, first, if it
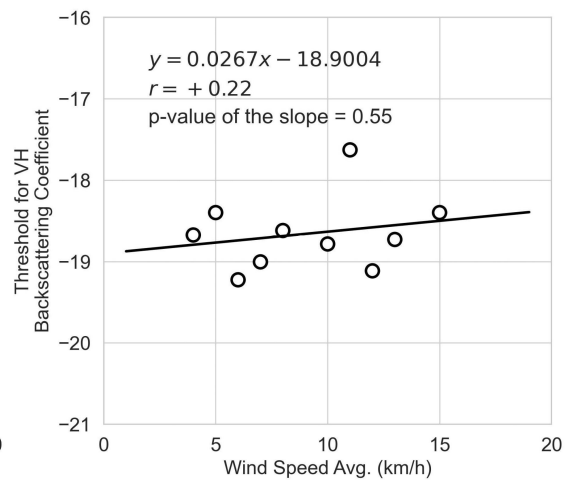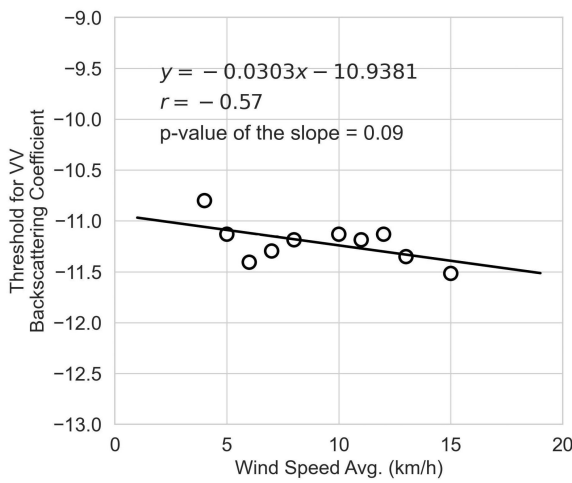
TABLE VIII
LINEAR RELATIONSHIP BETWEEN WIND SPEED AVG. AND THRESHOLD FOR VV AND VH POLARIZATIONS DURING THE COLD MONTHS (A) AND THE WARM
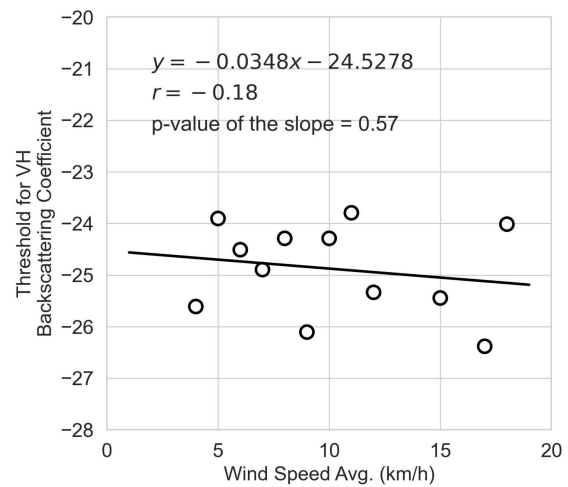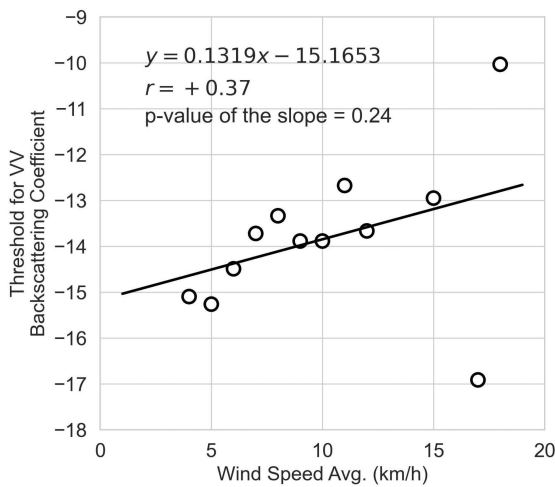MONTHS (B)

(a) Cold months.

Wind Speed Avg. (km/h)	VV Thresholds	VH Thresholds
4	-10.80	-18.67
5	-11.13	-18.40
6	-11.41	-19.22
7	-11.30	-19.00
8	-11.19	-18.62
10	-11.13	-18.78
11	-11.19	-17.63
12	-11.13	-19.11
13	-11.35	-18.73
15	-11.52	-18.40

(b) Warm months.

Wind Speed Avg. (km/h)	VV Thresholds	VH Thresholds
4	-15.10	-25.61
5	-15.26	-23.90
6	-14.49	-24.51
7	-13.72	-24.89
8	-13.33	-24.29
9	-13.88	-26.11
10	-13.88	-24.29
11	-12.67	-23.79
12	-13.66	-25.34
15	-12.95	-25.45
17	-16.91	-26.38
18	-10.03	-24.01

(a)

(b)

Fig. 5.   Relationship Between Wind Speed and Threshold for VV and VH Polarizations during the (a) cold months and the (b) warm months.
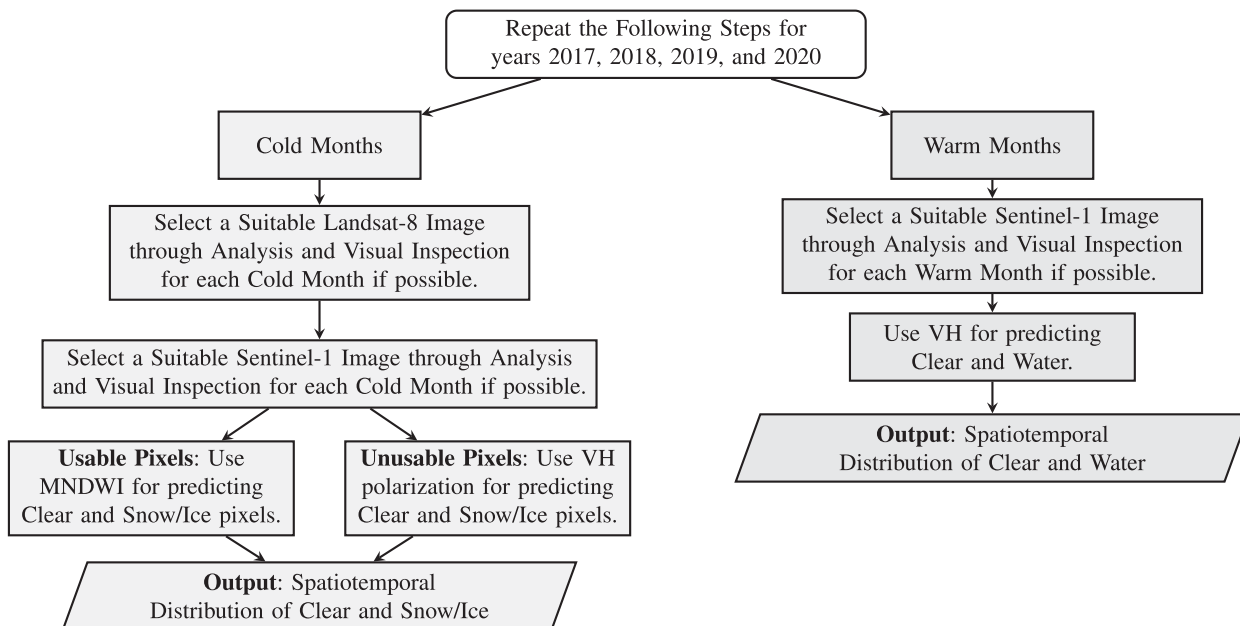
Fig. 6. Workflow of generating spatiotemporal distribution of clear, water, and snow/Ice.

was possible, a Landsat-8 image for each month was selected through analysis and visual inspection. Then, for each month, a Sentinel-1 image whose acquisition date was the closest to the previously selected Landsat-8 image from the same month was chosen. Thus, a Landsat-8 image and/or Sentinel-1 image for each month was found (except for January 2017 as there was no usable image for this month) from 2017 to 2021.

As illustrated in Tables VI and VII, the threshold-based classifications for separating clear and snow/ice pixels utilizing VV and VH polarizations were not as reliable as the classifications through the multispectral indices. Consequently, an image fusion algorithm was developed for separating clear and snow/ice pixels during the cold months. The algorithm first applied the threshold classification method utilizing MNDWI on the shortlisted Landsat-8 images. For the remaining pixels, the algorithm applied the threshold classification method using VH polarization on the shortlisted Sentinel-1 images. However, during the warm months, for separating clear and water pixels, the algorithm only used the shortlisted Sentinel-1 images for a threshold classification through the VH polarization coefficient. A summary of the workflow is available in Fig. 6.

IV. RESULTS AND DISCUSSION

As described earlier, the Landsat-8 and Sentinel-1 images listed in Tables III and IV were used for determining the thresholds for separating clear and snow/ice pixels during the cold months and clear and water pixels during the warm months. The following subsections demonstrate the change map and validation results.
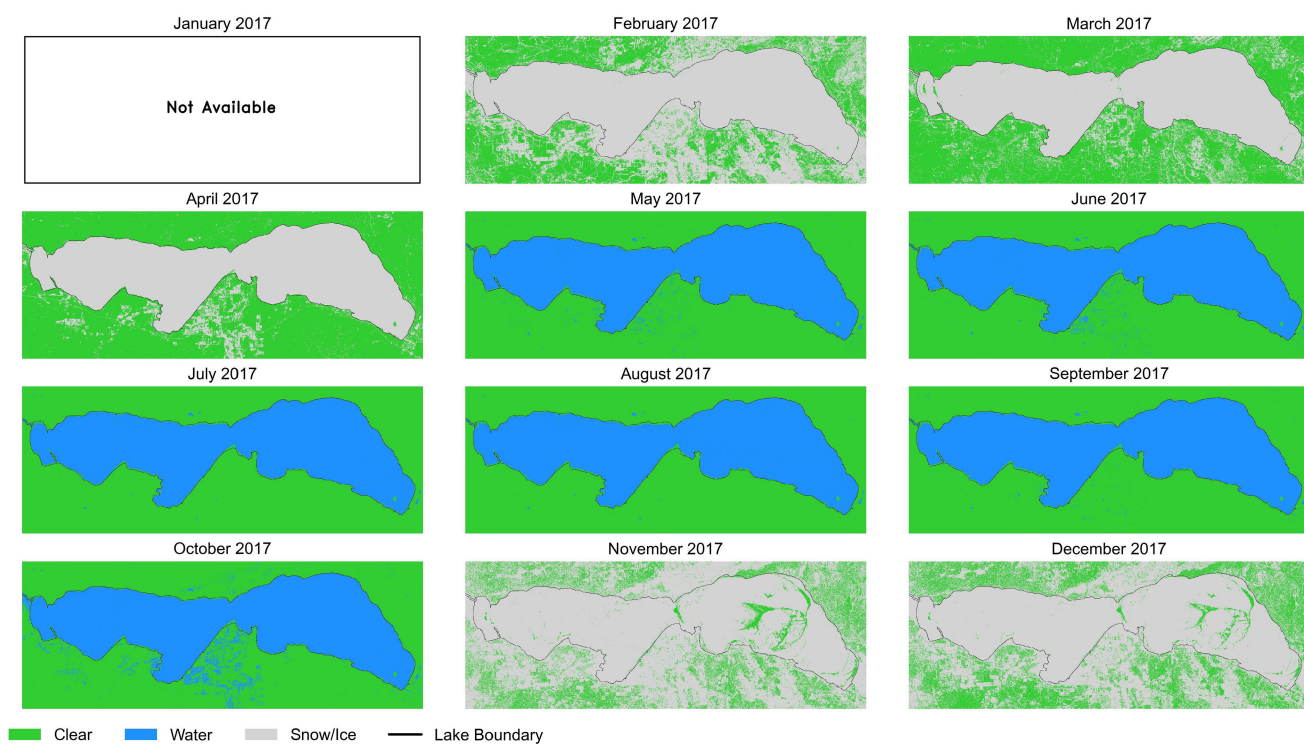
A. Interannual Water Area Dynamics

Fig. 7 illustrates the spatiotemporal distribution of clear, water, and snow/ice at Lesser Slave Lake based on MNDWI and

VH polarization from 2017 to 2021. As is evident, during the cold months, most of the lake surface and the region under study mostly was covered by snow/ice. In addition, Table IX summarizes the output of our fusion algorithm for the years 2017, 2018, 2019, and 2020. In this table, Landsat-8 % and Sentinel-1 %, respectively, show the percentage of each image used for generating the final spatiotemporal distributions through fusion.

The threshold-based classification method was employed to split water and clear pixels within the lake boundaries during the warm months. The changes in monthly accumulated precipitation and surface water area of the Lesser Slave Lake from 2017 to 2021 during the warm months are summarized in Table X. The monthly accumulated precipitation was the largest in July 2017 and 2019 and in June 2018 and 2020. Likewise, the water surface area was the largest in June 2018 and 2020; however, it was the largest in May 2017 and 2019. Noting that the precipitation is not generally in direct relation to water surface extend, this anomaly could have been caused as the result of human activities, such as industrial activities and agricultural crop rotations. Fig. 8 shows the spatiotemporal distribution of surface water at Lesser Slave Lake from 2017 to 2021 during the warm months. As can be seen, the water area of the lake remained almost steady during the warm months of these four years (2017–2020).

Further insights are provided in Fig. 9. This figure shows monthly accumulated precipitation for the lake during the warm months from 2017 to 2021. Observe that the precipitation, overall, was highest during June and July. Furthermore, the surface water area of the Lesser Slave Lake for the same period is also available in Fig. 9. The surface water area was higher in 2020 than those in 2017–2019. In addition, the monthly discharge rate for S5 during the warm months of 2018 and 2019 is also displayed in Fig. 9. As already indicated in Section I, the datasets for only these two years were available. The discharge
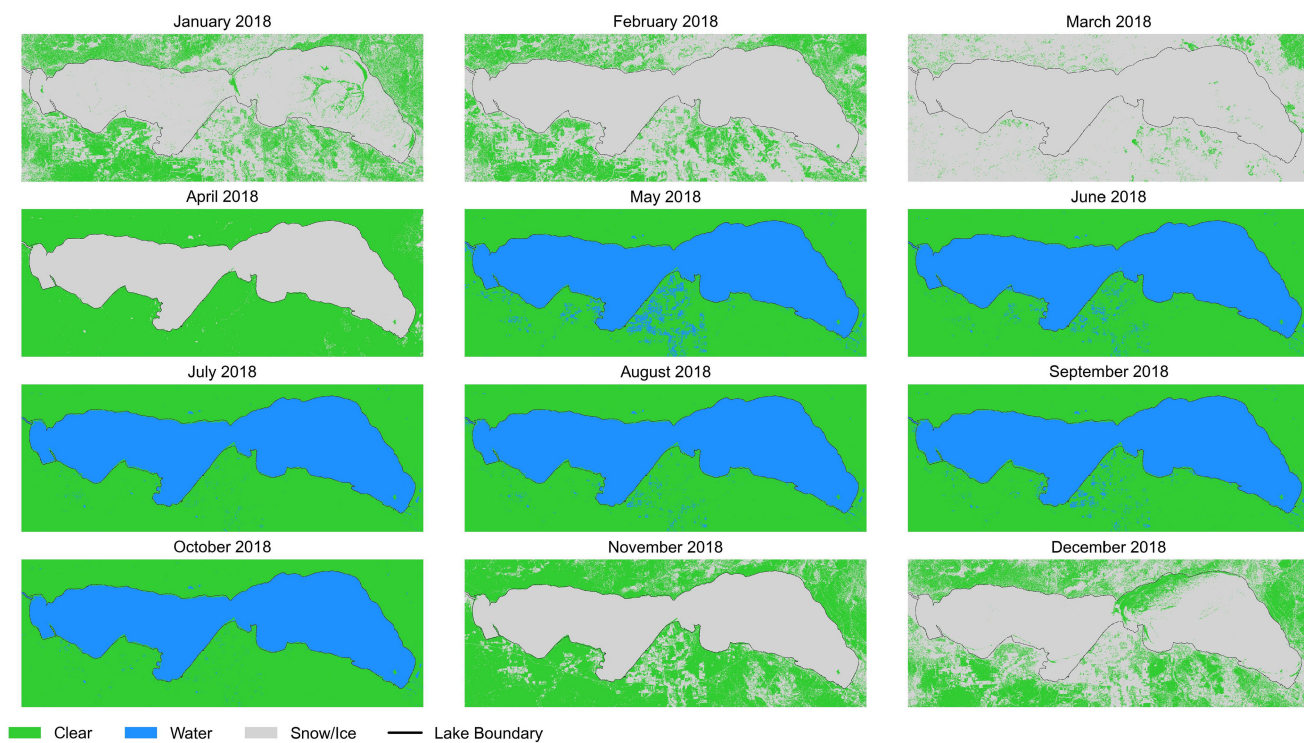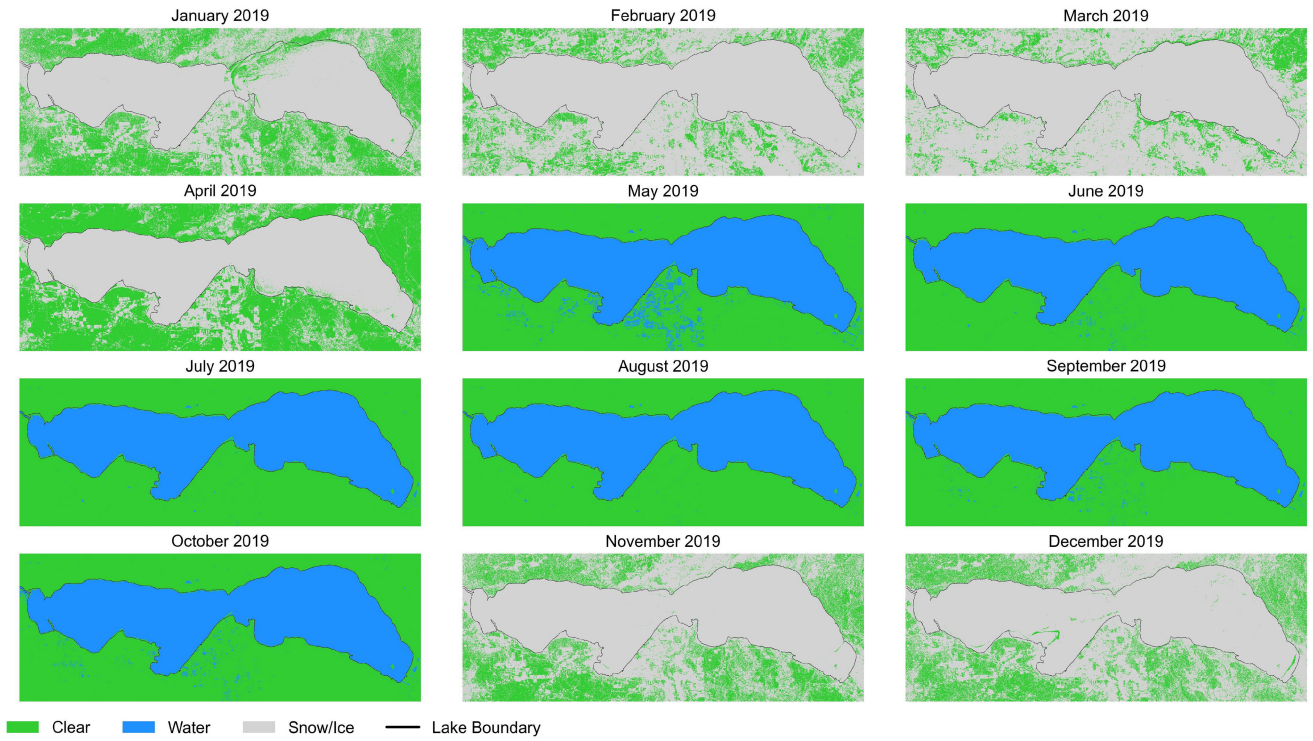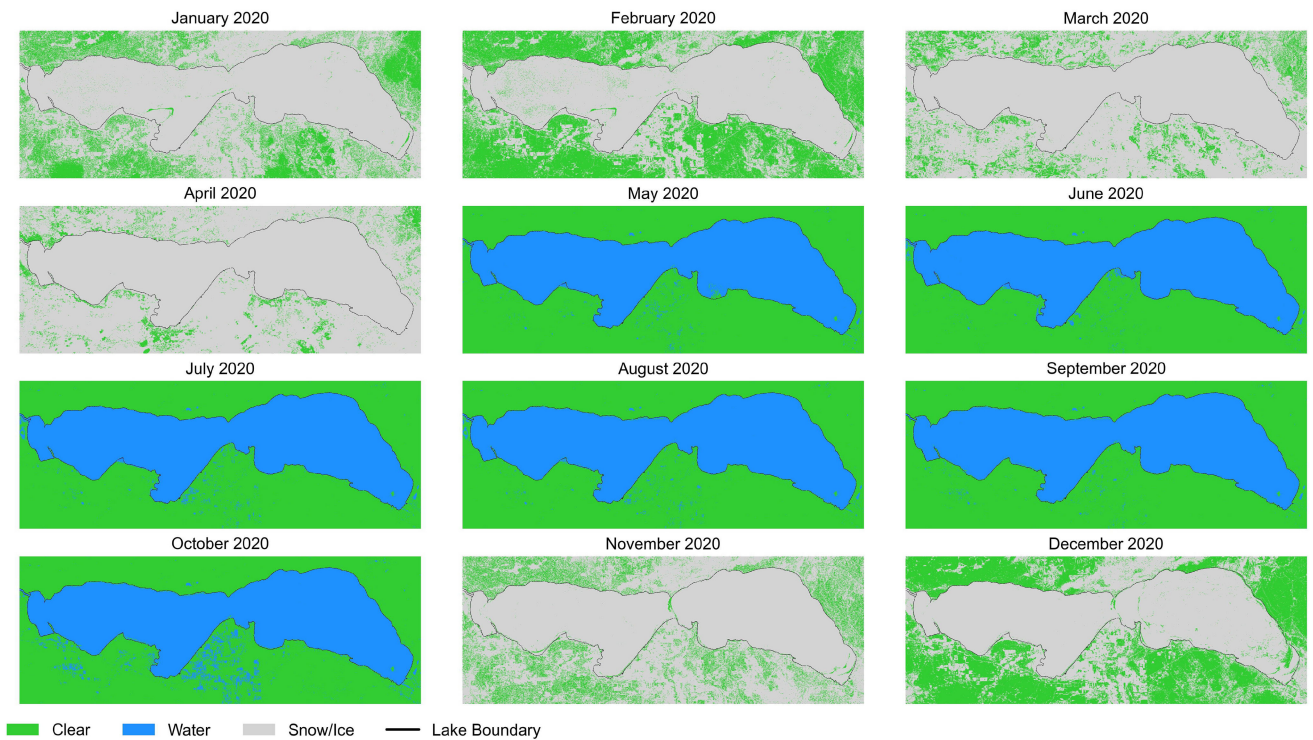
Fig. 7.   Spatiotemporal distribution of Clear, Water, and Snow/Ice at Lesser Slave Lake based on MNDWI and VH polarization for 2017 (a) and 2018 (b).

(c)

(d)

Fig. 7. *(Continued)* Spatiotemporal distribution of Clear, Water, and Snow/Ice at Lesser Slave Lake based on MNDWI and VH polarization for 2019 (c) and 2020 (d).

TABLE IX
CLEAR, WATER, AND SNOW/ICE SURFACE DISTRIBUTION AT LESSER SLAVE LAKE IN 2017, 2018, 2019, AND 2020

Month	2017		2018		2019		2020	
	Landsat-8 Image %	Sentinel-1 Image %	Landsat-8 Image %	Sentinel-1 Image %	Landsat-8 Image %	Sentinel-1 Image %	Landsat-8 Image %	Sentinel-1 Image %
January	-	-	0.00	100.00	0.00	100.00	0.00	100.00
February	76.79	23.21	81.73	18.27	97.43	2.57	0.00	100.00
March	53.63	46.37	97.52	2.48	95.04	4.96	94.36	5.64
April	0.00	100.00	94.05	5.95	0.00	100.00	93.57	6.43
May	0.00	100.00	0.00	100.00	0.00	100.00	0.00	100.00
June	0.00	100.00	0.00	100.00	0.00	100.00	0.00	100.00
July	0.00	100.00	0.00	100.00	0.00	100.00	0.00	100.00
August	0.00	100.00	0.00	100.00	0.00	100.00	0.00	100.00
September	0.00	100.00	0.00	100.00	0.00	100.00	0.00	100.00
October	0.00	100.00	0.00	100.00	0.00	100.00	0.00	100.00
November	0.00	100.00	0.00	100.00	0.00	100.00	0.00	100.00
December	0.00	100.00	0.00	100.00	0.00	100.00	0.00	100.00

TABLE X
CHANGES IN THE AVERAGE MONTHLY ACCUMULATED PRECIPITATION (M) AND THE SURFACE WATER AREA OF THE LESSER SLAVE LAKE DURING THE WARM MONTHS FROM 2017 TO 2021

Year	Month	Accumulated Precipitation (mm)	Water Area (km^2)	Year	Month	Accumulated Precipitation (mm)	Water Area (km^2)
2017	May	50.71	1142.29	2018	May	17.35	1148.22
	June	83.27	1140.13		June	139.36	1151.63
	July	120.18	1135.24		July	91.14	1142.26
	August	37.60	1132.70		August	53.23	1144.22
	September	66.56	1136.99		September	44.37	1139.91
	October	51.44	1142.28		October	27.31	1142.63
2019	May	10.44	1149.17	2020	May	59.69	1153.46
	June	91.92	1144.35		June	126.00	1158.15
	July	168.61	1142.86		July	90.95	1157.82
	August	72.94	1145.58		August	43.11	1153.00
	September	46.96	1144.75		September	14.21	1151.24
	October	51.17	1147.50		October	39.13	1151.99

data did not show a significant correlation with our estimated surface water area which can be explained by the complex structure of the lake, human activity, and climate change. The average monthly water level (from station S4) for the lake during the warm months from 2017 to 2020 is also shown in Fig. 9. The monthly averaged water level was only available at S4 located in the southwest region of the lake. However, the water level value measured at the outlet is not a reliable indicator of the water surface extent. We could not investigate the long-term surface water/ice dynamics (i.e., decadal) due to the lack of valid Landsat-8 imagery in certain months and the availability of frequent Sentinel-1 data only for the period of 2017–2020.

B. Investigating Other Approaches

A great amount of effort has been made to implement various deep learning and machine learning methods for obtaining accurate pixel water surface proportion information through remote sensing. Isikdogan et al. in [32] proposed a model, named Deep-WaterMap, that learned the attributes of water bodies from data drawn from across the globe. Their model could be used for separating water from land, snow, ice, clouds, and shadows using only Landsat-8 datasets. Moreover, Pham-Duc et al. developed a neural network classification model utilizing Landsat-8 and

Sentinel-1 dataset [12]. Their model could be implemented for separating water and nonwater pixels.

A summary of some other methods, investigated for separating clear and snow/ice during pixels in the cold months and separating clear and water pixels during the warm months, is provided in this section. Various binary classifications were executed including various Scikit-learn APIs [33], [34], such as support vector machines (SVMs), decision trees (DTs), and ensemble methods that combine several base models to produce one optimal predictive model. Several deep learning models were exercised including Tensorflow APIs [35], Pytorch APIs [36], and CatBoost APIs [37]. However, these methods only improved the accuracy metrics from threshold classifications insignificantly (our classifications accuracy metrics are available in Tables VI and VII). Therefore, a simple yet effective method was presented herein: the threshold-based classification.

One of the main challenges that we faced during the threshold-based classifications, through machine learning and deep learning methods, is that the lake and the land in the region of interest were heavily covered by snow during cold months. It was nearly impossible to separate clear and snow/ice pixels efficiently through classifications mainly by utilizing VV and VH polarizations. To improve the accuracy of such models, during the cold months, we may require Landsat-8 and Sentinel-1 images from the same day to include other climate parameters such as wind speed, precipitation, and temperature.

Fig. 8.   Spatiotemporal distribution of surface water at Lesser Slave Lake from 2017 to 2021 during the warm months.

V. Conclusion

In this article, the surface water area of Lesser Slave Lake was estimated for May, June, July, August, September, and October (referred as the warm months) from 2017 to 2021. As demonstrated, for the rest of the months of each year (the cold months), the surface of the lake and most of the region under study were covered by snow/ice. A fusion method that utilizes threshold classifications for separating clear and water pixels during the warm months and separating clear and snow/ice during the cold months was used.

Landsat-8 and Sentinel-1 images were resampled at 30-m spatial resolution for training the threshold-based classification method. We identified that MNDWI for Landsat-8 and VH for Sentinel-1 had the best weighted-average score and overall accuracy score among other indices during the cold months with, respectively, 92.10% and 68.86% overall accuracies. Similarly, we found that NDWI and VH had excellent overall accuracies of
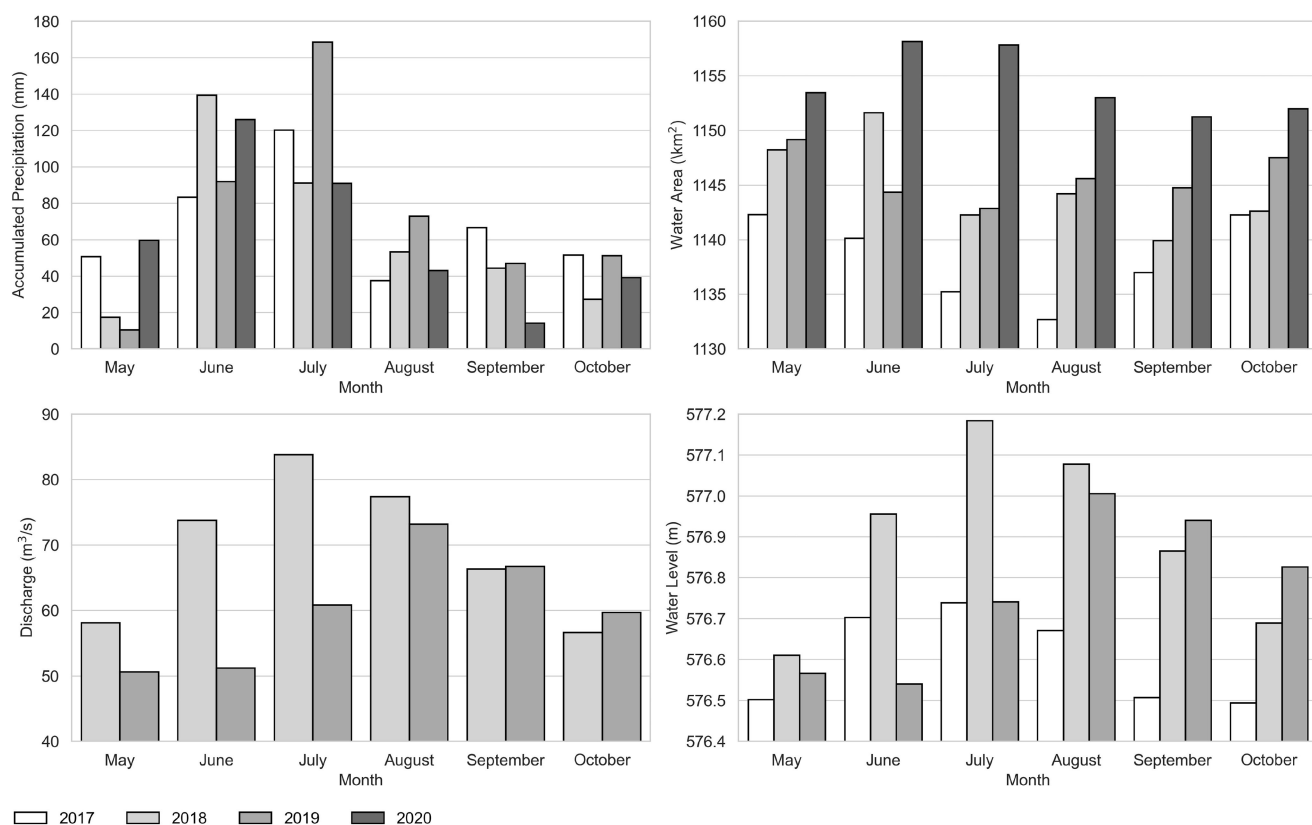
Fig. 9.   Changes in the monthly precipitation (mm), monthly surface water area of the Lesser Slave Lake (km ^{2}), monthly averaged discharge (m^3 / s) measured at station S5, and monthly averaged water level (m above the mean sea level) measured at station S4 from 2017 to 2021 during the warm months.

99.88% and 98.49% during the warm months, respectively. The water level measured at the S4 outlet, illustrated in Fig. 1, neither showed the surface dynamics of the lake nor was a reliable indicator of the water volume of the lake. Therefore, the use of remote sensing imagery is highly recommended for studying water resources and the influence of climate change and human activity on them.

Limitations of this study include the lack of valid Landsat-8 imagery in certain months and the availability of frequent Sentinel-1 data only for the period of 2017–2020. Therefore, the long-term surface water/ice dynamics (i.e., decadal) were not investigated here. Furthermore, there did not exist any Landsat-8 imagery that was partly covered by ice and partly covered by water for training the model to delineate double thresholds for the described multispectral and SAR indices. Therefore, we relied on the weather data and defined cold and warm months with the assumption of either water or snow/ice in these months.

REFERENCES

[1] T. Kutser, D. C. Pierson, K. Y. Kallio, A. Reinart, and S. Sobek, "Mapping lake CDOM by satellite remote sensing," *Remote Sens. Environ.*, vol. 94, no. 4, pp. 535–540, 2005.

[2] M. E. Hereher, "Environmental monitoring and change assessment of Toshka lakes in southern Egypt using remote sensing," *Environ. Earth Sci.*, vol. 73, no. 7, pp. 3623–3632, 2015.

[3] C. Pipitone, A. Maltese, G. Dardanelli, M. Lo Brutto, and G. La Loggia, "Monitoring water surface and level of a reservoir using different remote sensing approaches and comparison with dam displacements evaluated via GNSS," *Remote Sens.*, vol. 10, no. 1, 2018, Art. no. 71.

[4] I. Klein, U. Gessner, A. J. Dietz, and C. Kuenzer, "Global WaterPack–a 250m resolution dataset revealing the daily dynamics of global inland water bodies," *Remote Sens. Environ.*, vol. 198, pp. 345–362, 2017.

[5] R. Luo, Q. Yuan, L. Yue, and X. Shi, "Monitoring recent lake variations under climate change around the Altai mountains using multimission satellite data," *IEEE J. Sel. Topics Appl. Earth Observ. Remote Sens.*, vol. 14, pp. 1374–1388, 2020.

[6] S. Lu, N. Ouyang, B. Wu, Y. Wei, and Z. Tesemma, "Lake water volume calculation with time series remote-sensing images," *Int. J. Remote Sens.*, vol. 34, no. 22, pp. 7962–7973, 2013.

[7] Y. Hu, J. Huang, Y. Du, P. Han, and W. Huang, "Monitoring spatial and temporal dynamics of flood regimes and their relation to wetland landscape patterns in Dongting lake from MODIS time-series imagery," *Remote Sens.*, vol. 7, no. 6, pp. 7494–7520, 2015.

[8] N. Xu, Y. Ma, W. Zhang, X. H. Wang, F. Yang, and D. Su, "Monitoring annual changes of lake water levels and volumes over 1984–2018 using Landsat imagery and ICESat-2 data," *Remote Sens.*, vol. 12, no. 23, 2020, Art. no. 4004.

[9] U. Bhangale, S. More, T. Shaikh, S. Patil, and N. More, "Analysis of surface water resources using Sentinel-2 imagery," *Procedia Comput. Sci.*, vol. 171, pp. 2645–2654, 2020.

[10] S. K. McFeeters, "The use of the normalized difference water index (NDWI) in the delineation of open water features," *Int. J. Remote Sens.*, vol. 17, no. 7, pp. 1425–1432, 1996.

[11] H. Xu, "Modification of normalised difference water index (NDWI) to enhance open water features in remotely sensed imagery," *Int. J. Remote Sens.*, vol. 27, no. 14, pp. 3025–3033, 2006.

[12] B. Pham-Duc, C. Prigent, and F. Aires, "Surface water monitoring within Cambodia and the vietnamese Mekong delta over a year, with Sentinel-1 SAR observations," *Water*, vol. 9, no. 6, 2017, Art. no. 366.

[13] J. W. Rouse et al., "Monitoring vegetation systems in the great plains with ERTS," *NASA Special Publication*, vol. 351, no. 1974, 1974, Art. no. 309.

[14] E. Ghaderpour, A. Ben Abbes, M. Rhif, S. D. Pagiatakis, and I. R. Farah, "Non-stationary and unequally spaced NDVI time series analyses by the LSWAVE software," *Int. J. Remote Sens.*, vol. 41, no. 6, pp. 2374–2390, 2020.

[15] E. Ghaderpour and T. Vujadinovic, "The potential of the least-squares spectral and cross-wavelet analyses for near-real-time disturbance detection within unequally spaced satellite image time series," *Remote Sens.*, vol. 12, no. 15, 2020, Art. no. 2446.

[16] B. Brisco, N. Short, J. v. d. R. Sanden Landry, and D. Raymond, "A semi-automated tool for surface water mapping with RADARSAT-1," *Can. J. Remote Sens.*, vol. 35, no. 4, pp. 336–344, 2009.

[17] M. Santoro, U. Wegmüller, C. Lamarche, S. Bontemps, P. Defourny, and O. Arino, "Strengths and weaknesses of multi-year envisat ASAR backscatter measurements to map permanent open water bodies at global scale," *Remote Sens. Environ.*, vol. 171, pp. 185–201, 2015.

[18] J. Reschke, A. Bartsch, S. Schlaffer, and D. Schepaschenko, "Capability of C-band SAR for operational wetland monitoring at high latitudes," *Remote Sens.*, vol. 4, no. 10, pp. 2923–2943, 2012.

[19] L. Xing, X. Tang, H. Wang, W. Fan, and G. Wang, "Monitoring monthly surface water dynamics of Dongting lake using Sentinel-1 data at 10m," *PeerJ*, vol. 6, 2018, Art. no. e4992.

[20] B. L. Parlee, K. Geertsema, and A. Willier, "Social-ecological thresholds in a changing boreal landscape: Insights from cree knowledge of the Lesser Slave Lake region of Alberta, Canada," *Ecol. Soc.*, vol. 17, no. 2, 2012, Art. no. 20.

[21] E. Ghaderpour, T. Vujadinovic, and Q. K. Hassan, "Application of the least-squares wavelet software in hydrology: Athabasca river basin," *J. Hydrol.: Regional Stud.*, vol. 36, 2021, Art. no. 100847.

[22] D. P. Roy et al., "Landsat-8: Science and product vision for terrestrial global change research," *Remote Sens. Environ.*, vol. 145, pp. 154–172, 2014.

[23] K. Sayler, "Landsat 8 collection 1 (C1) land surface reflectance code (LaSRC) product guide," Dept. Interior U.S. Geological Surv., Reston, VA, USA, LSDS-1368 Version 3.0, 2020.

[24] E. T. Mitchard et al., "Mapping tropical forest biomass with radar and spaceborne LiDAR in lopé national park, gabon: Overcoming problems of high biomass and persistent cloud," *Biogeosciences*, vol. 9, no. 1, pp. 179–191, 2012.

[25] W. Huang et al., "Automated extraction of surface water extent from Sentinel-1 data," *Remote Sens.*, vol. 10, no. 5, 2018, Art. no. 797.

[26] G. R. Terrell and D. W. Scott, "Variable kernel density estimation," *Ann. Statist.*, vol. 20, no. 3, pp. 1236–1265, 1992.

[27] V. A. Epanechnikov, "Non-parametric estimation of a multivariate probability density," *Theory Probability Its Appl.*, vol. 14, no. 1, pp. 153–158, 1969.

[28] D. W. Scott, *Multivariate Density Estimation: Theory, Practice, and Visualization*. Berlin, Germany: Wiley, 2015.

[29] M. J. Warrens, "Cohen's kappa is a weighted average," *Stat. Methodol.*, vol. 8, no. 6, pp. 473–484, 2011.

[30] D. Powers, "Evaluation: From precision, recall and f-measure to ROC, informedness, markedness & correlation," *J. Mach. Learn. Technol.*, vol. 2, no. 1, pp. 37–63, 2011.

[31] J. Lee Rodgers and W. A. Nicewander, "Thirteen ways to look at the correlation coefficient," *Amer. Statistician*, vol. 42, no. 1, pp. 59–66, 1988.

[32] F. Isikdogan, A. C. Bovik, and P. Passalacqua, "Surface water mapping by deep learning," *IEEE J. Sel. Top. Appl. Earth Observ. Remote Sens.*, vol. 10, no. 11, pp. 4909–4918, Nov. 2017.

[33] F. Pedregosa et al., "Scikit-learn: Machine learning in python," *J. Mach. Learn. Res.*, vol. 12, pp. 2825–2830, 2011.

[34] L. Buitinck et al., "API design for machine learning software: Experiences from the scikit-learn project," in *Proc. ECML PKDD Workshop: Lang. Data Mining Mach. Learn.*, 2013, pp. 108–122.

[35] M. Abadi et al., "TensorFlow: A system for large-scale machine learning," in *Proc. 12th USENIX Symp. Operat. Syst. Des. Implement.*, 2016, pp. 265–283. [Online]. Available: https://www.tensorflow.org/about/bib

[36] A. Paszke et al., "Pytorch: An imperative style, high-performance deep learning library," *Adv. Neural Inf. Process. Syst.*, vol. 32, pp. 8026–8037, 2019.

[37] L. Prokhorenkova, G. Gusev, A. Vorobev, A. V. Dorogush, and A. Gulin, "CatBoost: Unbiased boosting with categorical features," in *Proc. Adv. Neural Inf. Process. Syst.*, 2018, vol. 31. [Online]. Available: https://proceedings.neurips.cc/paper/2018/hash/14491b756b3a51daac41c24863285549-Abstract.html

Hatef Dastour received the the Ph.D. degree in applied mathematics in 2019 with the University of Calgary, Calgary, AB, Canada, where he is currently working toward the second Ph.D. degree in geomatics engineering.

His research interests include highly accurate and efficient numerical methods for various industrial problems, big data analytics, and the application of data science in remote sensing data, and climate data analytics.

Ebrahim Ghaderpour received the first Ph.D. degree in theoretical and computational science from the University of Lethbridge, Lethbridge, Canada, in 2014, and the second Ph.D. degree in earth and space science from York University, Toronto, Canada, in 2018. He completed two postdoctoral appointments with the Departments of Mathematics and Statistics and Geomatics Engineering, University of Calgary.

He is currently an Assistant Professor with the Department of Earth Sciences, Sapienza University of Rome, Rome, Italy, and also the CEO of Earth and Space Inc. His research interests include big data analytics, in particular, satellite and climate data analytics.

Quazi K. Hassan received the B.Sc. degree in electrical and electronics engineering from the Khulna University of Engineering and Technology, Bangladesh in 1994, the M.Sc. degree in civil engineering from University Putra Malaysia, Seri Kembangan, Malaysia, in 1998, and the Ph.D. degree in remote sensing and ecological modelling from the University of New Brunswick, Fredericton, Canada, in 2008.

He is a Professor with the Department of Geomatics Engineering, University of Calgary, Calgary, AB, Canada. His research interests include the application of remote sensing in forecasting and monitoring of natural hazards/disasters, such as forest fire, drought, and flooding; use of remote sensing and GIS techniques in understanding the dynamics of natural resources, such as forestry, agriculture, and water; and integration of remote sensing, GIS, and modeling techniques in addressing issues related to energy and environment.